X-ray spectroscopy on the active ion in laser crystals

P. S. Miedema,[a†] R. Mitzner,[a] S. Ganschow,[b] A. Föhlisch[a,c] and M. Beye[a†]

The active ions in typical laser crystals were studied with Resonant Inelastic X-ray Scattering (RIXS) and Partial Fluorescence Yield X-ray Absorption (PFY-XAS) spectroscopies as solid state model systems for dilute active centers. We analyzed Ti^{3+} and Cr^{3+} in α-Al_2O_3:Ti^{3+} and $LiCaAlF_6$:Cr^{3+} respectively. The comparison of experimental data with semi-empirical multiplet calculations provides insights into the electronic structure and shows how measured crystal field energies are related across different spectroscopies.

1. Introduction

Active transition metal centres in a relatively inactive matrix are widespread in biology, (bio)chemical and technological applications, e.g., in enzymes, in catalysis[1], or as part of photoactive molecules in solution[2–5]. Such diluted systems can be uniquely studied with X-ray spectroscopies that are intrinsically element specific by addressing core levels. Here, the soft x-ray regime (~40 – 1400 eV) features the sharpest available core levels for all the elements in the Periodic Table[6] and thus allows for highest energy resolution in electronic structure determination. Among the soft x-ray spectroscopies, especially resonant inelastic x-ray scattering (RIXS) is a very powerful technique[7–9] and can be viewed as a combination of x-ray absorption spectroscopy (XAS), to study unoccupied states, and x-ray emission spectroscopy (XES) addressing occupied valence bands.

Recently, studies of dilute molecules in liquids with RIXS (with about 0.1-1 mole/L)[2,10–13] have been performed in addition to the more standard studies of bulk solid materials. Due to limited signal levels and thus required long-term stability, it remains difficult to perform soft X-ray RIXS at very low concentrations in liquids.

In this article we use the dopants in solid state laser crystals as dilute active centre with concentrations below (0.1 at%) and similar to (3 at%) generally applied for liquids. We support our RIXS measurements with multiplet simulations and compare the results to available optical data. Similarities and differences in the respectively obtained electronic structure information are discussed.

2. Experimental and theoretical methods

2.1 Sample preparation

The titanium sapphire α-Al_2O_3:~0.1 at%Ti^{3+} (TiSa) crystal was obtained from Saint-Gobin crystals produced for usage in laser amplifiers[14,15], where at% refers to the atomic percentage of Al substitution by Ti. The crystal was cut down to about 1 millimetre thickness and repolished before the measurements.

The $LiCaAlF_6$:Cr^{3+} (LiCAF:Cr^{3+}) single crystal was grown using the Czochralski technique with radio-frequency induction heating. The starting material, stoichiometric or near-stoichiometric mixtures of the metal fluorides, was melted in 40 ml Pt or Pt/Au crucibles in a gas flow of 5N nitrogen with < 2 ppm residual H_2O gas content. Small amounts of NH_4HF_2 were added to the mixture in order to react with adsorbed water at elevated temperature before melting[16,17]. Chromium concentration in the melt was up to 3 at% with respect to Al. Since the segregation coefficient is known to be near unity[18], chromium distribution in the crystals must be expected to be homogeneous at the level of melt doping. Crystallization was initiated by pulling a seed crystal immersed into the melt upwards at simultaneous lowering of the heating power. The seed was suspended from a balance, detecting changes in the crystal weight used for the automatic diameter control. Crystals were pulled with a rate of 1.0 millimetre/h and continuously rotated to improve melt mixing and compensate for azimuthal thermal inhomogeneities caused e.g. by observation windows. The grown crystals were 18 millimetre in diameter and up to 100 millimetre long, of intense green colour and free of obvious defects like cracks, massive inclusions or similar. Prior to the measurements, the crystals were cut into millimetre thin pieces and polished.

2.2 X-ray spectroscopy experiment

The spectra of these samples were measured with the SolidFlexRIXS-setup featuring a Nordgren-type Graze-spectrometer[19] fixed in the horizontal plane at 90° to the incoming beam. We used beamline U49/2-PGM-1[20] of the synchrotron Bessy-II of the Helmholtz-Zentrum Berlin. The incident energy resolution was 0.4-0.5 eV and the spectrometer resolution was set to about 0.4 eV. The L-edge X-ray absorption spectra of the dopants were measured by summing the total 3d emission signal as a function of excitation energy often referred to as 3d-partial fluorescence yield (PFY) x-ray absorption. The PFY and RIXS experiments have been performed with linear horizontal polarized x-ray excitation under an incidence angle of about 40 degrees to the surface. A typical RIXS map was measured in about 3 hours. For the Cr^{3+}, with more features to resolve, four of such measurements were added up to increase statics and no beam damage was observed on these time scales. All measurements were performed at room temperature.

2.3 Crystal field multiplet theory

We applied calculations in the crystal field approximation taking local electronic 3d-electron interactions into account. With Quanty[21] we simulated $L_{2,3}$-edge RIXS and 3d-PFY-XAS,

where the TT-multiplet code developed by Theo Thole[22], based on the Cowan code[23] and additions by Butler et al.[24], was used to provide the input for the Hartree-Fock Slater integrals and the atomic 3d spin-orbit coupling. These crystal field simulations were performed for the active 3d-metal ion, here with the electronic configurations of [Ar]$3d^1$ for Ti^{3+} and [Ar]$3d^3$ for Cr^{3+}. Since our $L_{2,3}$-edge measurements induce transitions between 2p and 3d orbitals, we usually refer to the relevant subset of ground state occupations: $2p^6 3d^1$ for Ti^{3+} and $2p^6 3d^3$ for Cr^{3+}. In our simulations, these ions were placed in an imagined crystal field with octahedral (O_h) symmetry, splitting the energy levels of the valence 3d orbitals into a threefold degenerate t_{2g} and a twofold degenerate e_g subset. The energetic difference between electrons in those subsets is referred to as 10Dq and is marked in Figure 1 in red.

Since X-ray absorption probes the core-excited state, there can be a reaction of the surroundings to the core excitation leading to a change in the crystal field and that is why we introduced a separate crystal field parameter for the core-excited state ($10Dq_{ES}$). We iteratively varied this parameter to agree with the experimental x-ray absorption spectrum. Deviations from the true XAS through using the partial fluorescence yield method have been accounted for in the simulations[25]. In addition, the x-ray absorption spectrum shows multiplet structures due to 2p-3d and 3d-3d interactions, which are taken into account in our simulations by the Slater integrals calculated in the Hartree-Fock approximation. In general, this approximation overestimates the Slater integrals, which can be accounted for by scaling the Hartree-Fock values with β=0.8 in accordance with Cowan's findings[23] to compensate for many-electron correlation effects not taken into account in the Hartree-Fock approximation. We point out that the CTM4XAS interface implicitly applies this scaling[9] and that simulations on oxides within CTM4XAS result often in a 0.7-0.8 scaling, which would be in our case a β of (0.8*0.8=) 0.64 or (0.7*0.8=) 0.56. This β-parameter can be reduced further to account for deviations from the purely ionic bonding through covalency effects that delocalize the 3d-electrons with the orbitals of neighbouring atoms leading to decreased 3d-3d electron interaction integrals.

In our simulations, we optimized both β and $10Dq_{ES}$ to match the experimental PFY-XAS spectra. We note that β mainly influences relative intensities and energy separations along the exciting photon energy axis as represented in PFY-XAS, with only minor influence on the spectral shape of RIXS spectra recorded at fixed photon energy for our model systems.

In the experimental samples, the Cr^{3+} and Ti^{3+} dopant ions are distributed randomly over various sites in the crystal resulting in nearly random relative orientations. Therefore isotropic PFY-XAS and RIXS simulations were applied, even though, as mentioned in section 2.2, the x-ray spectroscopy experiments were performed with linear horizontal polarized x-ray excitation under an incidence angle of about 40 degrees to the surface and the detector placed in the horizontal scattering plane perpendicular to the beam. All states that were within 0.02 eV from the observed initial ground state were taken into account in the self-consistent field cycle for the ground state electronic structure. The actual RIXS and PFY-XAS simulations were performed on only the (four-fold-degenerate for both Ti^{3+} and Cr^{3+}) ground state. All simulations were Lorentzian broadened with 0.5 eV.

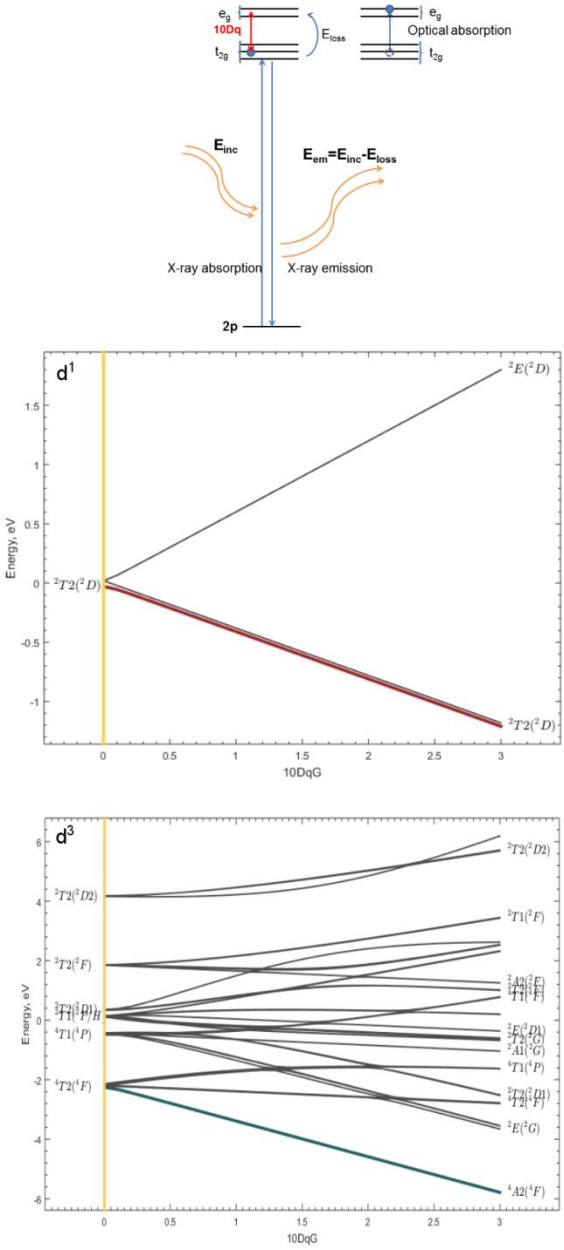

Figure 1. The RIXS process (top) and Tanabe-Sugano diagrams constructed with CTM4DOC[26] for Ti^{3+} (d^1, middle panel) and Cr^{3+} (d^3, lowest panel) providing possible optical 3d-3d excitations. Incoming X-rays with the energy E_{inc} are absorbed by exciting a 2p electron to an empty 3d level. Radiative decays fill the 2p core level while emitting x-rays with energy E_{em}. The energy difference (E_{loss}) between the x-ray absorption (E_{inc}) and the x-ray emission (E_{em}) is connected to an excitation in the system, for example between t_{2g} and e_g states. The crystal field energy 10Dq is marked as the transition of an electron from a t_{2g} orbital to an e_g orbital. A 3d-3d excitation measured with optical absorption in UV/vis spectroscopy (right) directly corresponds to the energy loss in RIXS. Excited 3d-3d states that can be reached through absorption / RIXS energy loss for Ti^{3+} and Cr^{3+} are presented in the Tanabe-Sugano diagrams in the middle and lowest panel where colored red and blue lines represent the ground state. The gerade symbols for O_h symmetry are omitted from the state assignments.

2.4 Linking 3d-3d excitations in RIXS with UV/vis spectroscopy

For a transition metal in an O_h crystal field, typically the excitation from a t_{2g} orbital into an e_g orbital is one of the lowest possible electronic excitations visible, usually located in the UV/vis energy region and yields the value of 10Dq as for the single 3d-electron in Ti^{3+}. One may expect as well intra-t_{2g} 3d-3d excitations (see Tanabe-Sugano diagram for a singly occupied 3d orbital (d^1) in Figure 1) due to 3d spin orbit interaction, but these appear rather weak and are commonly not observed experimentally within typical resolutions because the 3d spin-orbit coupling is of the order of 50 meV. In general though, dipole transitions between the orbitals of the same subshell are forbidden, following the selection rules ($\Delta L=\pm1$, $\Delta S=0$). Nevertheless, 3d-3d excitations often weakly appear in UV/vis spectra because of phonon coupling for octahedral systems or by removal of the g/u character in non-centrosymmetric sites (in non-octahedral systems). Therefore the octahedral 10Dq can be extracted, albeit with potential modification through the coupling.

In contrast to optical absorption, RIXS involves two dipole transitions – absorption followed by emission – as in resonantly enhanced Raman spectroscopy. Excitations in the material are encoded in the energetic difference between the two (see Fig. 1). In such a Raman process, 3d-3d excitations are dipole-allowed and RIXS can for example directly measure 10Dq in the ground state without the necessity to couple to phonons.

3. Results and discussion

We will first describe the experimental and theoretical Ti $L_{2,3}$-edge RIXS obtained for TiSa and Cr $L_{2,3}$-edge RIXS obtained for LiCAF:Cr^{3+}. After that we discuss the PFY-XAS results for both compounds.

3.1 Ti $L_{2,3}$-edge RIXS of TiSa

Following the considerations in section 2.4, the first energy loss feature in the RIXS spectra of Ti^{3+} that is sufficiently separated from the elastic emission should directly yield 10Dq. We used our measurements to fix this $10Dq_{initial}$ as the crystal field splitting of the ground state and simulated the RIXS spectra accordingly. UV/vis finds a 10Dq of 2.23 eV for TiSa[14]. The $10Dq_{initial}$ of 2.2 eV found in the RIXS experiment agrees well within the measurement resolution. In the x-ray absorption process of Ti^{3+}, a 2p electron is excited into the unoccupied 3d manifold ($2p^63d^1 \rightarrow 2p^53d^2$), thereby allowing for 3d-3d (and 2p-3d) interactions in the core-excited state. Multiple structures appear in the spectrum as function of photon energy (e.g., see Figure 6 and Figure 7 later on) and the shape of the x-ray absorption spectrum depends strongly on 10Dq[27,28]. However, in the initial and final state of RIXS, the filled 2p shell and the single 3d electron do not allow for such interactions. Only one certain 3d-3d excitation remains for a $3d^1$ system within our experimental resolution (ignoring the possible intra-t_{2g} excitations at very low energy as seen in the Tanabe-Sugano diagram of d^1 in Figure 1): the t_{2g}-e_g excitation remains visible in the experimental (and simulated) spectrum which directly corresponds to the energetic value of 10Dq.

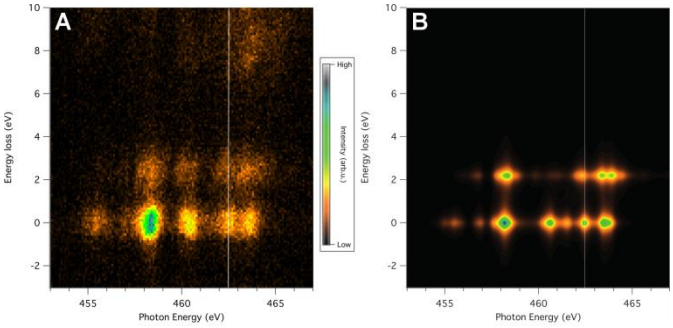

Figure 2. A) Experimental Ti $L_{2,3}$-edge RIXS map of TiSa with energy loss (vertical axis) versus exciting photon energy (horizontal axis) B) Ti $L_{2,3}$-edge RIXS map calculated with the parameters $10Dq_{initial}$=2.2 eV, $10Dq_{ES}$=1.98 eV and β=0.55. The simulation results are shifted in exciting photon energy by 458.7 eV. The white vertical lines mark the slices shown in Figure 3.

Figure 2 shows the comparison of the experimental and simulated Ti $L_{2,3}$-edge RIXS maps of TiSa while Figure 3 shows one vertical slice of these RIXS maps and the energies match but the intensity and broadening is different. Features above an energy loss of 5 eV only appear in the experimental spectrum and can be related to charge transfer excitations, which are not taken into account in our simulations. They could be reproduced by explicitly accounting for charge transfer between the metal ion and the ligands[8,9] but do not contain further information on the optical activity of the ion.

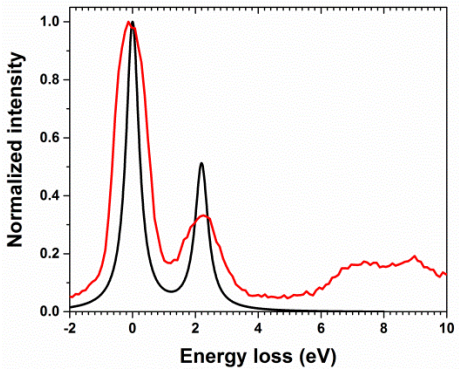

Figure 3. RIXS slices of the RIXS maps in Figure 2 at an excitation energy of 462.5 eV as function of energy loss from the simulated Ti $L_{2,3}$ RIXS map in Figure 2B (black) and the experimental RIXS taken from Figure 2A (red).

3.2 Cr $L_{2,3}$-edge RIXS of LiCAF:Cr^{3+}

Figure 4 shows the experimental and simulated Cr $L_{2,3}$ RIXS maps of LiCAF:Cr^{3+}. More features are visible as compared to the Ti^{3+} maps in Figure 2. Now, multiplet interactions of Cr^{3+} ($3d^3$) in both the ground state (3d-3d interactions) as well as in the x-ray excited state (2p-3d and additional 3d-3d interactions) appear. The first resolved RIXS transition can be again be identified with a t_{2g}-e_g transition with energy of 10Dq (see Figure 1 lowest panel: ^2E_g and $^4T_{1g}$ are the first 3d-3d excitations which refer to t_{2g}-e_g excitations).

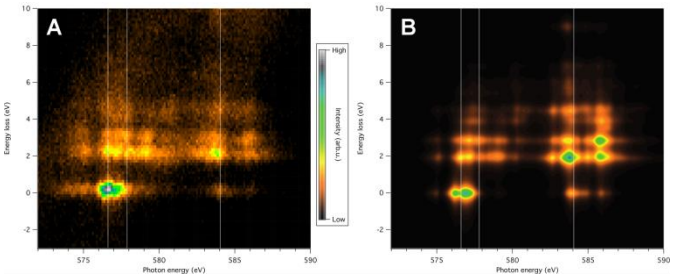

Figure 4. A) Experimental Cr $L_{2,3}$-edge RIXS map of $LiCaAlF_6:Cr^{3+}$ with energy loss (vertical axis) versus exciting photon energy (horizontal axis). B) Cr $L_{2,3}$-edge RIXS map calculated with the parameters $10Dq_{initial}$=1.9 eV, $10Dq_{ES}$=1.71 eV and β=0.75. The simulated results are shifted in photon energy by 578 eV. The white vertical lines mark the slices shown in Figure 5.

In the experimental RIXS we find a value for 10Dq of 1.9 eV in agreement with other data[15,29,30]: This value is in between experimental and theoretical optical data of 1.83 eV and 2.02 eV for excitations from the ground initial state $^4A_{2g}$ to the ^2E_g and $^4T_{1g}$ state (see as well the Tanabe-Sugano diagram for d^3 in Figure 1) respectively[29]. From other literature on optical studies of $LiCAF:Cr^{3+}$ it is known that $10Dq_{initial}$~2.0 eV[15,30].
Figure 5 provides a more detailed comparison of the experiment and the theoretical simulation by RIXS slices taken from the simulated and experimental Cr $L_{2,3}$-edge RIXS maps of LiCAF: Cr^{3+} and of the simulation of Cr^{3+} with $10Dq_{initial}$=1.9 eV, $10Dq_{ES}$=1.71 eV and β=0.75.

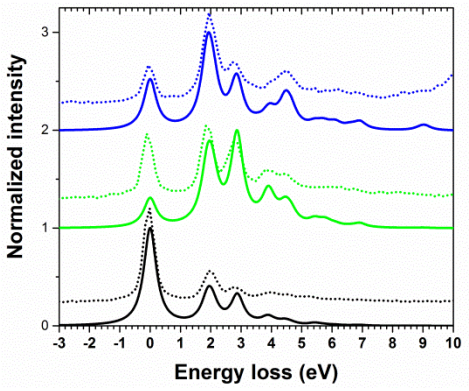

Figure 5. RIXS slices at photon energies of 576.8 eV (black), 577.9 eV (green) and 584.2 eV (blue) as function of energy loss from the simulated Cr $L_{2,3}$ RIXS map in Figure 4B (solid lines) and from the experimental Cr $L_{2,3}$ RIXS map in Figure 4A (dotted lines).

In contrast to TiSa, the various multiplet interactions yield energy loss features that extend up to about 10 eV. Only at about 9-10 eV, broader features appear in the experiment (e.g., the blue dotted line) due to charge transfer excitations. The simulations reproduce all other features. For some RIXS slices the relative intensity of the elastic line differs between experiment and simulation (compare the green lines), but the inelastic features can be reproduced both in relative intensity as well as peak position.

In order to match the full RIXS map with structures in both the energy loss features as well as along the exciting photon energy axis, we had to introduce different crystal field parameters for the ground and the core excited states. With the ground state 10Dq fixed by the first excitation in the RIXS spectra, we now analyze in the PFY-XAS how 10Dq of the core-excited state ($10Dq_{ES}$) is determined.

3.3 TiSa PFY-XAS

Figure 6 shows the Ti $L_{2,3}$-edge PFY-XAS of TiSa (blue line) in comparison to some simulations of a Ti^{3+} ion in O_h symmetry using different values for 10Dq. It becomes apparent that using the same crystal field parameters for RIXS and XAS ($10Dq_{initial}=10Dq_{ES}$=2.2eV) does not agree well enough yet with the measured absorption spectrum. Especially around 461.5 eV the simulation yields intensity in an additional feature, which is not prominent in the experiment. Best agreement with the experimental data is found for 10Dq=1.98 eV, a 90% scaling of the ground state value (red line, Figure 6). A deviating $10Dq_{initial}$ of 2.2 eV to match the RIXS data above, while keeping $10Dq_{ES}$=1.98 eV (green line, Figure 6) does not influence the absorption spectrum (compare the red and the green lines in Figure 6: these are equivalent).

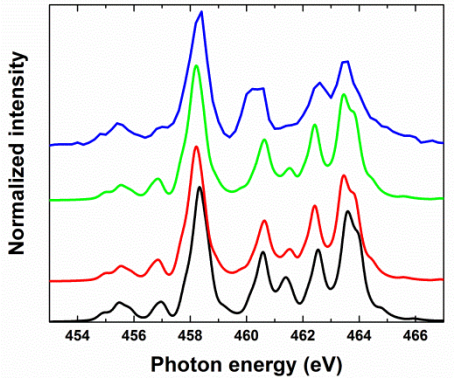

Figure 6. Ti $L_{2,3}$-edge partial fluorescence yield (PFY) x-ray absorption spectrum (XAS) of Ti^{3+}:α-Al_2O_3 (TiSa, top, blue) compared to simulations of Ti^{3+} in O_h symmetry with $10Dq_{initial}=10Dq_{ES}$=2.2 eV and β=0.55 (black), $10Dq_{initial}=10Dq_{ES}$=1.98 eV and β=0.55 (red), and $10Dq_{initial}$=2.2 eV, $10Dq_{ES}$=1.98 eV and β=0.55 (green). All simulated spectra are broadened with 0.5 eV Lorentzian broadening.

We have also verified how distortions from octahedral symmetry affect the PFY-XAS, since tetragonal or trigonal distortions from O_h symmetry to D_{4h} (or D_{3d}) symmetry appear in Ti $L_{2,3}$-edge x-ray absorption spectra of Ti^{4+}-containing minerals[31] and a trigonal distortion is reported for TiSa[32,33]. We simulate an analogous situation by introducing additional parameters on top of 10Dq: We use an additional splitting Δ_1 between the t_{2g} orbital energies and Δ_2 between the e_g orbital energies. Although the fundamental parameters for particular D_{4h} or D_{3d} symmetry distortions are Ds, Dt or Dσ, Dτ, we just aimed to simulate the resulting effect on the splitting of the 3d-orbitals, which directly encodes in the Δ_1 and Δ_2 parameters. We noticed that the agreement between simulations and experiment becomes worse with strong distortion. For small distortion, the spectral changes are below our experimental resolution. Therefore it is concluded that within the experimental accuracy of our soft x-ray $L_{2,3}$-edge PFY-XAS and RIXS experiments, the Ti^{3+} can be regarded as being in an O_h symmetric surrounding.
Using the Hartree-Fock Slater integral scaling parameter β to mimic the degree of covalency and match relative peak

positions and intensities, best agreement for TiSa is found with β=0.55(+/-0.05) and all presented simulations for Ti^{3+} use this value.

3.4 LiCAF:Cr3+ PFY-XAS

In Figure 7 the same analysis is shown for the Cr $L_{2,3}$-edge PFY-XAS of LiCAF:Cr^{3+}. With the simulations we demonstrate, also here, optimal agreement for a 90% scaling of the ground state value $10Dq_{ES}$=1.71 eV=0.9*$10Dq_{initial}$ creating best agreement around 579 eV and 584 eV (compare with black vertical lines).
We further observed again no indication of a distorted symmetry from O_h Thus again, best match between simulation and experiment is found for an undistorted O_h symmetry within our experimental accuracy. A difference between the two crystals is identified in optimizing the β parameter: best agreement is achieved for LiCAF:Cr^{3+} with a value of 0.75 as opposed to the 0.55 found for TiSa. This confirms the intuitively expected larger ionic character of fluorine ligands as compared to more covalent oxygen ligands.

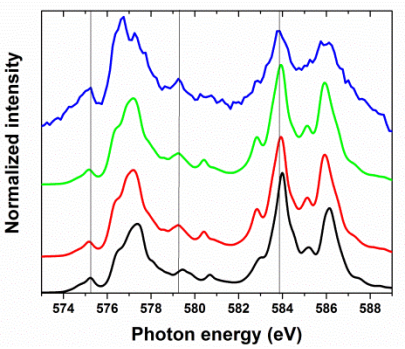

Figure 7. Cr $L_{2,3}$-edge partial fluorescence yield (PFY) x-ray absorption spectra (XAS) of $LiCaAlF_6:Cr^{3+}$ (top, blue) compared to simulations with $10Dq_{initial}$=$10Dq_{ES}$=1.9 eV and β=0.75 (black), $10Dq_{initial}$=$10Dq_{ES}$=1.71 eV and β=0.75 (red), $10Dq_{initial}$=1.9, and $10Dq_{initial}$=1.9, $10Dq_{ES}$=1.71 eV and β=0.55 (green). All simulated spectra are broadened with 0.5 eV Lorentzian broadening. Vertical black lines mark peaks of the experimental PFY-XAS.

3.5 Discussion on symmetry distortion sensitivity

Based on our experimental data and theoretical analysis, it seems that soft X-ray $L_{2,3}$-edge (PFY-)XAS is thus less sensitive to local symmetry distortions than metal K-edge x-ray absorption natural linear dichroism (XNLD) or hard X-ray pre-edge XAS/RIXS as seen for example for iron systems[34–36]. For a deeper analysis of distortions, polarization-dependent XAS, e.g., XNLD[37] and hard x-ray K-edge RIXS[34] are more sensitive than the soft x-ray $L_{2,3}$-edge RIXS experiments provided here, since those techniques have been shown to be able to identify different types of distortion[34]. However XNLD and 1s2p RIXS remain excited-state probes, so without further data it would be unclear if the observed distortion comes from the actual probe x-ray excitation or if the distortion is already present in the ground state (before x-ray absorption), while the soft X-ray $L_{2,3}$-edge RIXS is capable of finding the ground state properties and the optical excited states without possible x-ray induced changes. With better energy resolution for $L_{2,3}$-edge RIXS one might actually be able to provide more information on symmetry distortion, since additional 3d-3d excitations might become visible with better energy resolution. On the other hand, for the $L_{2,3}$-edge PFY-XAS, the appearance of many multiplet features makes it less sensitive to small symmetry distortions, while large symmetry distortions (for our simulations Δ_1 or Δ_2 > 0.5 eV) can be picked up by both $L_{2,3}$-edge PFY-XAS and RIXS as we observed in our simulations (not presented here).

3.6 Discussion on $10Dq_{initial}$ vs $10Dq_{ES}$

The trend of observing a lower $10Dq_{ES}$ in XAS than in the ground state ($10Dq_{initial}$) has previously been observed[38], for example in a comparison of UV/vis, TDDFT simulations and $L_{2,3}$-edge RIXS on cobalt compounds[39,40] and this observation is rationalized by a reaction of the ligand field to the excitation of an electron from a local 2p to a more delocalized 3d state. In addition to the previous results we actually quantified the decreased $10Dq_{ES}$ in XAS as compared to $10Dq_{initial}$ for two different systems: Using a scaling of 90%, we propose here a general rule of thumb to connect ground state $10Dq_{initial}$ as relevant for optical excitations with values obtained from element specific X-ray absorption spectroscopy.

3.7 Discussion on RIXS maps versus RIXS cuts

For the relatively simple diluted cases in this manuscript, a single RIXS cut would have been sufficient to obtain $10Dq_{initial}$. For more complex diluted systems (e.g., with lower symmetry or for systems with more 3d-electrons or with possible beam damage quickly arising) one may obtain a RIXS map to identify which 3d-3d excitations link to 10Dq and which to lower symmetry crystal field parameters. Especially consider the possibility that features may only appear at particular excitation energies. This might disturb the analysis when only a single RIXS cut has been measured at the wrong excitation energy. Therefore we recommend the use of RIXS maps in a first step to identify well-chosen excitation energies for RIXS cuts with more statistics.

4. Conclusions

In summary, we demonstrated the power of RIXS to study fundamental electronic structure parameters of dilute active metal ions embedded in an inactive matrix. By comparison with detailed calculations using the Quanty code, we find that O_h symmetry is a good approximation for the embedding crystal and validate the larger influence of covalency for oxygen ligands as compared to more ionic fluorine systems.
We further stress that RIXS is a superior probe for ground state electronic parameters as compared to XAS and XNLD, where x-ray excited parameters are observed or even optical spectroscopy. With the energy loss in RIXS one measures optical transitions (albeit with Raman selection rules) and one can directly relate to the ground state properties of the material relevant for its biological, chemical or photo-activity. As opposed to optical spectroscopy though, RIXS is element-selective and can thus disentangle influences from different active ions in more complex compounds. We further demonstrate that in contrast to RIXS, XAS measures an altered

crystal field parameter due to the reaction of the system to the core hole, although we also find that for both studied system this parameter can be scaled back to the ground state value.

Acknowledgements

We thank T. Blume for technical support of the SolidFlexRIXS-chamber and HZB for beamtime allocation. PSM thanks Prof. M. Haverkort for support with the Quanty simulations. The RIXS simulations of Quanty were performed on the Maxwell-cluster at DESY. MB acknowledges financial support from the Volkswagenstiftung. We further thank Christiane Förster for cutting the crystals prior to the experiment.

Notes and references

1 R. A. van Santen, P. W. N. M. van Leeuwen, J. A. Moulijn and B. A. Averill, Eds., *Catalysis: An Integrated Approach*, Elsevier Science B.V., Amsterdam, The Netherlands, 2nd, revis edn., 2000.

2 K. Kunnus, W. Zhang, M. G. Delcey, R. V Pinjari, P. S. Miedema, S. Schreck, W. Quevedo, H. Schroeder, A. Föhlisch, K. J. Gaffney, M. Lundberg, M. Odelius and P. Wernet, *JPCB*, 2016, **120**, 7182–7194.

3 M. Chergui, *Acc. Chem. Res.*, 2015, **48**, 801–808.

4 W. Zhang and K. J. Gaffney, *Acc. Chem. Res.*, 2015, **48**, 1140–1148.

5 P. Gütlich, Y. Garcia and H. A. Goodwin, *Chem. Soc. Rev.*, 2000, **29**, 419–427.

6 F. J. Himpsel, *Phys. Status Solidi*, 2011, **248**, 292–298.

7 L. J. P. Ament, M. van Veenendaal, T. P. Devereaux, J. P. Hill and J. van den Brink, *Rev. Mod. Phys.*, 2011, **83**, 705–767.

8 A. Kotani, *Eur. Phys. J. B*, 2005, **47**, 3–27.

9 F. de Groot and A. Kotani, *Core Level Spectroscopy of Solids*, 2008.

10 K. Kunnus, I. Rajkovic, S. Schreck, W. Quevedo, S. Eckert, M. Beye, E. Suljoti, C. Weniger, C. Kalus, S. Grübel, M. Scholz, D. Nordlund, W. Zhang, R. W. Hartsock, K. J. Gaffney, W. F. Schlotter, J. J. Turner, B. Kennedy, F. Hennies, S. Techert, P. Wernet and A. Föhlisch, *Rev. Sci. Instrum.*, 2012, **83**, 123109.

11 S. Schreck, A. Pietzsch, K. Kunnus, B. Kennedy, W. Quevedo, P. S. Miedema, P. Wernet and A. Föhlisch, *Struct. Dyn.*, 2014, **1**, 54901.

12 L. Weinhardt, E. Ertan, M. Iannuzzi, M. Weigand, O. Fuchs, M. Bär, M. Blum, J. D. Denlinger, W. Yang, E. Umbach, M. Odelius and C. Heske, *Phys. Chem. Chem. Phys.*, 2015, **17**, 27145–53.

13 L. Weinhardt, M. Blum, O. Fuchs, A. Benkert, F. Meyer, M. Bär, J. D. Denlinger, W. Yang, F. Reinert and C. Heske, *J. Electron Spectros. Relat. Phenomena*, 2013, **188**, 111–120.

14 P. F. Moulton, *J. Opt. Soc. Am. B*, 1986, **3**, 125–133.

15 W. T. Silfvast, *Laser Fundamentals*, Cambridge University Press, Cambridge, 2nd edn., 2004.

16 D. Klimm and P. Reiche, *Cryst. Res. Technol.*, 1998, **33**, 409–416.

17 D. Klimm and P. Reiche, *J. Cryst. Growth*, 2000, **210**, 683–693.

18 R. F. Belt and R. Uhrin, *J. Cryst. Growth*, 1991, **109**, 334–339.

19 J. Nordgren, G. Bray, S. Cramm, R. Nyholm, J.-E. Rubensson and N. Wassdahl, *Rev. Sci. Instrum.*, 1989, **60**, 1690.

20 T. Kachel, *J. large-scale Res. Facil.*, 2016, **2**, A72.

21 M. W. Haverkort, *J. Phys. Conf. Ser.*, 2016, **712**, 12001.

22 B. T. Thole, R. D. Cowan, G. A. Sawatzky, J. Fink and J. C. Fuggle, *Phys. Rev. B*, 1985, **31**, 6856–6858.

23 R. D. Cowan, *The Theory of Atomic Structure and Spectra*, University of California Press, Berkeley and Los Angeles, California, 1981.

24 P. H. Butler, *Point Group Symmetry Applications - Methods and Tables*, Plenum Press, New York, 1981.

25 P. S. Miedema, P. Wernet and A. Föhlisch, *PRA*, 2014, **89**, 52507.

26 M. U. Delgado-Jaime, K. Zhang, J. Vura-Weis and F. M. F. de Groot, *J. Synchrotron Radiat.*, 2016, **23**, 1264–1271.

27 F. M. F. de Groot, J. C. Fuggle, B. T. Thole and G. A. Sawatzky, *Phys. Rev. B*, 1990, **42**, 5459–5468.

28 G. van der Laan and I. W. Kirkman, *J. Phys. Condens. Matter*, 1992, **4**, 4189–4204.

29 L.-R. Yang, C.-F. Wei, Y. Mei and W.-C. Zheng, *J. Fluor. Chem.*, 2016, **189**, 39–42.

30 U. Demirbas, M. Schmalz, B. Sumpf, G. Erbert, G. S. Petrich, L. a Kolodziejski, J. G. Fujimoto, F. X. Kärtner and A. Leitenstorfer, *Opt. Express*, 2011, **19**, 20444–20461.

31 F. M. F. de Groot, M. O. Figueiredo, M. J. Basto, M. Abbate, H. Petersen and J. C. Fuggle, *Phys Chem Miner.*, 1992, **19**, 140–147.

32 E. Gaudry, D. Cabaret, P. Sainctavit, C. Brouder, F. Mauri, J. Goulon and A. Rogalev, *J. Phys. Condens. Matter*, 2005, **17**, 5467–5480.

33 D. S. McClure, *J. Chem. Phys.*, 1962, **36**, 2757.

34 M. Hunault, V. Vercamer, M. W. Haverkort, M.-A. Arrio, C. Brouder, G. Calas and A. Juhin, *J. Phys. Conf. Ser.*, 2016, **712**, 12005.

35 V. Vercamer, M. O. J. Y. Hunault, G. Lelong, M. W. Haverkort, G. Calas, Y. Arai, H. Hijiya, L. Paulatto, C. Brouder, M. Arrio and A. Juhin, *Phys. Rev. B*, 2016, **94**, 245115.

36 T. E. Westre, P. Kennepohl, J. G. Dewitt, B. Hedman, K. O. Hodgson and E. I. Solomon, *J. Am. Chem. Soc.*, 1997, **119**, 6297–6314.

37 A. Juhin, F. de Groot, G. Vankó, M. Calandra and C. Brouder, *Phys. Rev. B*, 2010, **81**, 115115.

38 S. P. Cramer, F. M. F. de Groot, Y. Ma, C. T. Chen, F. Sette, C. A. Kipke, D. M. Eichhorn, M. K. Chan, W. H. Armstrong, E. Libby, G. Christou, S. Brooker, V. McKee, O. C. Mullins and J. C. Fuggle, *JACS*, 1991, **113**, 7937–7940.

39 M. M. van Schooneveld, R. W. Gosselink, T. M. Eggenhuisen, M. Al Samarai, C. Monney, K. J. Zhou, T. Schmitt and F. M. F. De Groot, *Angew. Chemie (Int. ed.)*, 2013, **52**, 1170–1174.

40 M. M. van Schooneveld, A. Juhin, C. Campos-Cuerva, T. Schmitt and F. M. F. de Groot, *J. Phys. Chem. C*, 2013, **117**, 14398–14407.